

Article

# Thermal Mechanical Processing of Press and Sinter Al-Cu-Mg-Sn-(AlN) Metal Matrix Composite Materials

Gregory A. W. Sweet<sup>1</sup>, Mary A. Wells<sup>2</sup>, Alan Taylor<sup>3</sup>, Richard L. Hexemer<sup>3</sup>, Ian W. Donaldson<sup>3</sup> and Donald Paul Bishop<sup>1,\*</sup>

<sup>1</sup> Department of Mechanical Engineering, Dalhousie University, 1360 Barrington Street, Halifax, NS B3J 1Z1, Canada; Greg.Sweet@dal.ca

<sup>2</sup> Department of Mechanical and Mechatronics Engineering, University of Waterloo, 200 University Ave. W., Waterloo, ON N2L 3G1, Canada; MAWells@uwaterloo.ca

<sup>3</sup> GKN Powder Metallurgy, 2200 N. Opdyke Road, Auburn Hills, MI 48326, USA; alan.taylor@gkn.com (A.T.); Rich.Hexemer@gkn.com (R.L.H.); Ian.Donaldson@gkn.com (I.W.D.)

\* Correspondence: paul.bishop@dal.ca; Tel.: +1-902-494-1520

Received: 30 May 2018; Accepted: 18 June 2018; Published: 23 June 2018



**Abstract:** The forging of sintered aluminum powder metallurgy alloys is currently viewed as a promising industrial technology for the manufacture of complex engineered products. The powder metallurgy process facilitates the use of admixed ceramic particles to produce aluminum metal matrix composites. However, fundamental data on the thermal-mechanical response of commercially relevant powder metallurgy alloy systems under varying conditions of temperature and strain rate are lacking. To address this constraint, the current study investigates the thermal-mechanical processing response of a family of metal matrix composite materials that employ a commercially exploited base alloy system coupled with admixed additions of aluminum nitride. Industrially-sintered compacts were tested under hot compression using a Gleeble 3500 thermal-mechanical test system to quantify their flow behavior. The nominal workability was assessed as a function of material formulation, sintered preform condition, and processing parameters (temperature and strain rate). Optical metallography and electron backscatter diffraction were used to observe the grain evolution through deformation. Full densification was achieved for materials with ceramic concentrations of 2% volume or less. Zener-Hollomon constituent analyses were also completed to elucidate a more comprehensive understanding the flow behavior inherent to each material. Flow behavior varied directly with the sintered density, which was influenced by the concentration and nature of ceramic particulate.

**Keywords:** 2xxx aluminum alloy; powder metallurgy; thermal mechanical processing; forging; Zener-Hollomon; metal matrix composites

## 1. Introduction

Aluminum powder metallurgy (APM) is a well-established component manufacturing technique routinely adopted within the automotive sector. Conventional APM involves the compaction and subsequent sintering of blended aluminum alloy powders into coherent, near-net shape components. Successful commercial applications include the high-volume production of camshaft bearing caps, transmission components, and heat sinks, to name but a few. To capitalize on this momentum, sustained proliferation of APM-derived components requires the development of new materials and/or processing technologies that yield products with improved mechanical properties. In many instances, the ability to meet this goal is underpinned by the capacity to address key metallurgical

features common within APM materials. For instance, the starting aluminum powders employed are inevitably encased in an oxide layer [1] that exhibits high thermodynamic stability. Although this feature is partially disrupted through conventional powder metallurgy (PM) operations [2], it still persists as a semi-continuous feature within the sintered product [3]. Residual porosity is a secondary feature encountered in sintered APM materials. Both attributes provide crack initiation sites [4] to the detriment of several properties, including fatigue behavior and tensile ductility.

One approach that can be applied to mitigate the aforementioned defects is elevated temperature plastic deformation, in particular, hot forging (a.k.a. thermal mechanical processing (TMP)). Conventionally, hot forging begins with fully dense, simple-shaped (i.e., bar, cylinder, etc.) wrought or cast billets that are progressively formed into the desired geometry through multiple hits in a series of forging dies. A competing technology rooted in the PM sector is known as powder forging (PF). Here, powder is compacted into the requisite preform shape, which is then sintered and hot forged. Although predominantly utilized in ferrous applications for the production of PF connecting rods [5], the forging of APM preforms has been studied as well [6–10], albeit to a lesser degree. PF is particularly advantageous in that practitioners have a tremendous capacity to engineer the preform shape [11]. Hence, preform and final part geometry are designed concurrently such that material utilization is maximized while plastic flow in critical areas is sufficient to promote increased mechanical properties; non-critical areas can be designed such that they undergo minimal material flow, thereby limiting die wear [10]. Ultimately, this allows forging to be efficiently completed in a single uniaxial stroke [10] while plastic strain coupled with frictional forces invoke pore collapse [12], grain refinement [11], and the disruption of persistent oxide networks [3].

Successful PF requires intimate knowledge on the flow behavior of a sintered material for a breadth of forging and microstructural conditions. A Zener-Hollomon type of constitutive analysis is one of the modelling tools commonly implemented in such endeavors. Here, it is understood that for a deforming metal, the instantaneous flow stress,  $\bar{\sigma}$ , varies as:

$$\bar{\sigma} = f(\theta, \bar{\epsilon}, \dot{\epsilon}, S) \quad (1)$$

where  $\theta$  is the isothermal forging temperature,  $\bar{\epsilon}$  is the strain,  $\dot{\epsilon}$  is the strain rate, and  $S$  is a parameter representing material and microstructure [13]. The material and microstructural contributions to flow stress are principally dictated by composition, although many secondary effects such as porosity, age-hardened state, equilibrium/non-equilibrium conditions, and the presence of secondary phases, etc. can also bear significant influence [14]. The peak flow stress,  $\bar{\sigma}$ , is the maximum flow stress observed during deformation. For fixed material composition and fixed strain, a set of constituent values can be extracted that represent the systems forging behavior.

The Zener-Hollomon (Z-H) constituent analysis approach is especially well documented in aluminum hot deformation [14]. More specifically, the sinh version, as shown in (2), was selected for its flexibility in correlating data with extreme variations in  $Z$  values [14]. The relationship is as follows:

$$A(\sinh(\alpha\dot{\sigma}))^n = \dot{\epsilon} \exp\left(\frac{Q_{HW}}{RT}\right) = Z \quad (1)$$

where  $Q_{HW}$  is the activation energy of hot working ( $\text{kJ mol}^{-1}$ ),  $R$  is the ideal gas constant ( $8.314 \text{ kJ}\cdot\text{mol}^{-1}\cdot\text{K}^{-1}$ ),  $T$  is the absolute temperature (K), and  $Z$  is the Zener-Hollomon parameter. Material-dependent constituent parameters include the stress multiplier  $\alpha$  ( $\text{MPa}^{-1}$ ),  $n$ , and  $A$ . These constituents were derived in accordance with the technique outlined by Mosher et al. [9]. For a characterized material system, the peak flow stress value may be predicted using (3) [14]:

$$\sigma = \left(\frac{1}{\alpha}\right) \ln \left\{ \left(\frac{Z}{A}\right)^{1/n} + \left[ \left(\frac{Z}{A}\right)^{2/n} + 1 \right]^{1/2} \right\} \quad (2)$$

The activation energy of hot working correlates to the deformation behavior of a material, and gives a good comparison as to how different alloys respond to deformation under a variety of forging conditions. Higher activation energies are attributed to materials that show greater change in peak flow stress behavior with temperature. For example, the activation energy of pure aluminum is ~140–156 kJ/mol [14], which is remarkably similar to non-heat treatable 3003, 152 kJ/mol. However, higher  $Q_{HW}$  values are observed in systems that undergo precipitation hardening to achieve their strength (i.e., fully annealed 2004 aluminum exhibits a value of 154 kJ/mol whereas the same material in the solutionized state has an increased activation energy of 270 kJ/mol as a result of significant strengthening of the material due to dynamic precipitation (DPN) favored at low temperatures [15]). Indeed, gains in  $Q_{HW}$  are attributed to increased solute, precipitates, dispersoids, inclusions, and their effects on the retardation of dynamic recovery (DRV) [15]. Ceramic or dispersoid-bearing alloys also tend to exhibit relatively high activation energies. This was exemplified in the work of McQueen et al. when they determined that an extruded PM 2618 alloy strengthened with 10 and 20 vol %  $Al_2O_3$  had activation energies of 315 kJ/mol and 400 kJ/mol, respectively [16]. Here, the secondary phases imparted heterogeneous dislocation generation that substantially increased flow stresses at low temperatures. However, at elevated temperatures, DRV is sufficiently effective to cope with the added dislocations such that the observed flow stresses for a composite material can often approach those measured for an unreinforced counterpart [17].

The purpose of this study was to investigate the response of commercially relevant APM materials to TMP. Specifically, a family of 2xxx series metal-matrix composites (MMCs) was considered. The alloy used in this study was selected because of its current commercial relevance and potential proliferation through improved mechanical properties. Comparable 2xxx series APM components see current use in camshaft bearing caps as well as automotive automatic transmission retaining plates and planetary gear carriers. Of interest was the densification and flow stress behavior as a function of deformation temperature and strain rate. A variety of ceramic contents were investigated alongside the unreinforced base alloy to observe how they influenced hot deformation behaviour.

## 2. Materials and Methods

The materials of interest in this study were blended from a single base alloy composition coupled with concentrations of AlN as the ceramic additive. Nominally, the base alloy chemistry was 95 Al (U.S. Metal Powders, Inc., Palmerton, PA, USA), 3 Cu (U.S. Metal Powders, Inc., Palmerton, PA, USA), 1.5 Mg (Tangshan Weihao Magnesium Powder Co., Ltd., Qian'an, China) and 0.5 Sn (Ecka Granules GMBH., Furth, Germany) (in weight %); pertinent metal powder information is provided in Table 1. An admixed lubricant powder, Licowax C (Clariant, Muttenz, Switzerland), was blended in at 1.5 wt %. Admixed with the base alloy was one of two AlN ceramic powders (H.C. Starck, Munich, Germany), AlN-C (Coarse) and AlN-F (Fine). Included in the scope of this study were ceramic volume fractions of 0, 2, 5 and 10, for both AlN-C and AlN-F. These blends will be referred to in this report by a numerical prefix representing the volume percent ceramic, and a lettered suffix representing the ceramic type (i.e., 2C for 2 vol % AlN-C). These will be contrasted to the 'Base' system that indicates samples of the matrix alloy devoid of admixed AlN.

**Table 1.** Overview of the metallic powders employed.

ELEMENT	TYPE	PARTICLE SIZE ( $\mu\text{M}$ ) (D10, D50, D90)		
Aluminum	Elemental	37	99	250
Copper	50:50 Al:Cu Master Alloy	5	16	45
Magnesium	Elemental	28	32	48
Tin	Elemental	5	12	34

Blending of all powders was completed in Nalgene bottles using a Turbula T2-F powder mixer (Glen Mills, Clifton, NJ, USA) with a 40 min residence time. Homogenized blends were then pressed

once into cylindrical (15 mm diameter  $\times$  26 mm height) green compacts with a targeted density of 2.48 g/cc. An Instron model 5594-200HVL 1 MN load frame (Instron, Norwood, MA, USA) coupled with a floating die tool set was utilized for this purpose. Green compacts were then sintered once in an industrial belt furnace used in commercial APM manufacturing. The thermal cycle included a hold at 400 °C for 10 min for delubrication immediately prior to sintering at 600 °C for 15 min. The sintering atmosphere was high purity nitrogen with a dew point between  $-55$  °C to  $-60$  °C and an oxygen concentration no higher than 5 ppm. Sintered specimens were subsequently machined into cylindrical samples that were 10 mm in diameter and 15 mm in height. Forging simulations were carried out on the machined cylinders in a Gleeble 3500 thermal-mechanical system (Dynamic Systems Inc., Poestenkill, NY, USA), seen in Figure 1, to a total strain of 0.70 mm/mm. Samples were individually loaded between two WC anvils (black arrows) and retained with a 50 N preload force. These uniaxial compression tests were completed using varied strain rates ( $5\text{ s}^{-1}$ ,  $0.5\text{ s}^{-1}$ ,  $0.05\text{ s}^{-1}$  or  $0.005\text{ s}^{-1}$ ) and isothermal temperatures (350 °C, 400 °C, 450 °C or 500 °C). All specimens were held at temperature for 15 s prior to loading to minimize temperature gradients. Additional tests were performed using an extended isothermal hold time of 150 s to investigate the effects of microstructural evolution prior to deformation. Strain values were measured using a diametrical “C” gauge, while temperature was controlled/monitored through a type-K thermocouple welded to the circumference of each test specimen equidistant from both compression anvils. Upon achieving a strain of 0.70 mm/mm samples were immediately and automatically water quenched to room temperature in an effort to preserve the microstructural features.

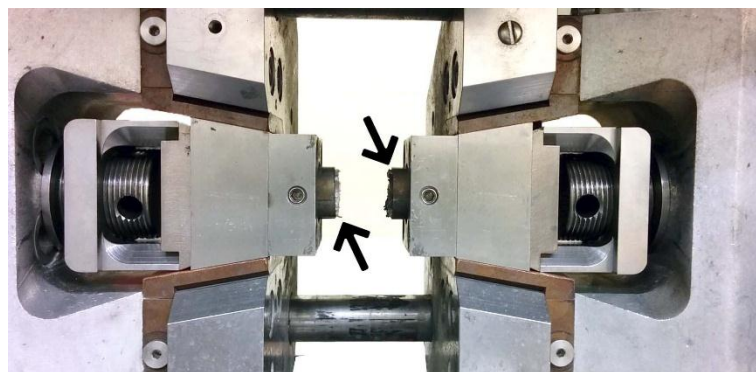


**Figure 1.** Gleeble 3500 anvil setup for hot compression testing.

Densities were measured before and after thermal mechanical processing using the Archimedes approach outlined in MPIF standard 42. These measurements were reported as a percentage of the full theoretical density for each respective material. Metallurgical examinations were performed on cold-mounted samples that were ground and polished through progressively finer SiC pads, diamond pastes, and finally, with colloidal silica media. Electron Backscatter Diffraction (EBSD) was performed on select samples in the as-polished state to investigate the nature of grains, subgrains and their boundaries. A Hitachi model S-4700 cold field SEM (Hitachi High-Technologies Co. Ltd., Tokyo, Japan) coupled with an HKL EBSD equipped with a Nordlys Oxford Instruments detector (Oxford Instruments, Abingdon, United Kingdom) was employed for this purpose. Backscatter electron micrographs of the aluminum phase for the relevant samples were also captured. Optical microscopy was performed with an Olympus BX51 light optical microscope (Olympus Corporation, Tokyo, Japan) on samples etched using Keller’s reagent unless otherwise noted. Error bars for relevant plotted data represent one standard deviation from the mean value obtained through measurements on no less than five unique samples.

### 3. Results

#### 3.1. Densification

Data on the density of samples before and after TMP are shown in Figure 2. The Base, 2C, and 2F compositions were sintered to near-theoretical (99.0% or better) densities. Hence, these relatively minor additions of AlN did not interfere with the sintering-induced densification behavior of the material to any meaningful extent. However, greater AlN contents, as exhibited by 5C, 10C, 5F, and 10F, proved that the as-sintered densities were measurably reduced through higher ceramic additions. Furthermore, the matrix alloy appeared to be more sensitive to the finer particle size AlN-F ceramic. In this sense, whereas 5C sintered to 98.4% of its theoretical potential, 5F only reached 96.1%. At higher concentration, density values are further compromised in a comparable fashion; 92.8% and 90.8% for 10C and 10F, respectively.

After hot deformation, the average density of a given material statistically exceeded that of the as-sintered counterpart in all instances. It was found that regardless of the temperature and strain rate conditions applied, the magnitude of density change was effectively identical. Accordingly, the ‘Forged’ values in Figure 2 represent the mean value of samples thermally and mechanically worked under the complete range of parameters considered. Through TMP, the alloys Base, 2C, and 2F densified by approximately 0.8% to 1.0%, achieving their theoretical maximum value. 5C exhibited densification of a similar magnitude, but failed to reach the theoretical maximum. The magnitude of density change for the alloys that exhibited a reduced sintered density was more significant. Here, 5C increased by 2.5% while 10C and 10F increased by 4.2% and 5.9%, respectively. Despite the density of as-sintered parts indicating AlN-C was the preferable ceramic for concentrations above 2%, there was no significant difference between the two after TMP.

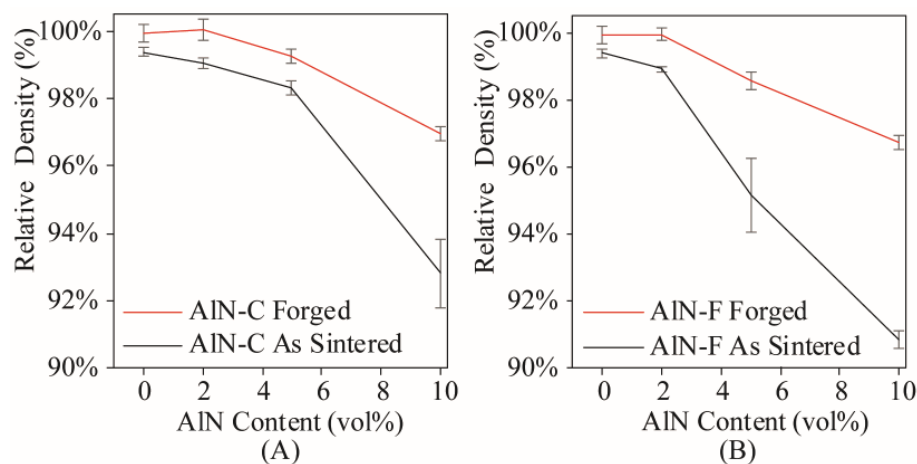


**Figure 2.** Densities of APM MMCs as measured before and after TMP. Materials prepared with (A) coarse and (B) fine AlN additions.

#### 3.2. Microstructural Transitions

Optical microstructures of all alloy systems in both the as-sintered and hot worked conditions are shown in Figure 3. The sequences A–D illustrate the nature of pores and how the porosity increases in the as-sintered base alloy (A) and coarse AlN alloys (B–D). Residual pores in the base system were rounded with a nominal size of 10  $\mu\text{m}$  to 25  $\mu\text{m}$ . Pores were solely located along prior particle boundaries. With additions of AlN, porosity persisted among AlN particles in addition to prior particle boundaries. Specifically, pores preferentially resided amongst clusters of relatively small ceramic particulate. With increased ceramic content, the number and diameter of AlN-adjacent pores increased. In the extreme case of 10C, pores exceeding 50  $\mu\text{m}$  as well as many finer ones persisted throughout the microstructure.

Akin to the pore development in the coarse AlN systems, the sintered microstructure of AlN-F alloys (Figure 3I–K) exhibited residual porosity associated with ceramic particulate. Moreover, the exclusively fine nature of the ceramic in these alloys drives additional residual porosity. In formulations 5F (Figure 3J) and 10F (Figure 3K) the ceramic phase decorates the aluminum interparticle boundaries semi-continuously. Much of the fine ceramic material in these regions appeared well incorporated with the matrix. During sintering, the liquid phase clearly wets the ceramic particles. However, the persistent large pores amongst AlN clusters indicated that sintering mechanisms were impeded. It may be that the interparticle ceramic interferes with mass transport in the crucial solution-reprecipitation phase of sintering. Another explanation may be that the volume of liquid phase was insufficient to both wet the additional ceramic surfaces while also effectively promoting conventional liquid phase sintering mechanisms. With increased AlN content, especially for finer AlN particles, the surface area which the liquid phase must wet increases dramatically, which would essentially tie up the liquid phase.

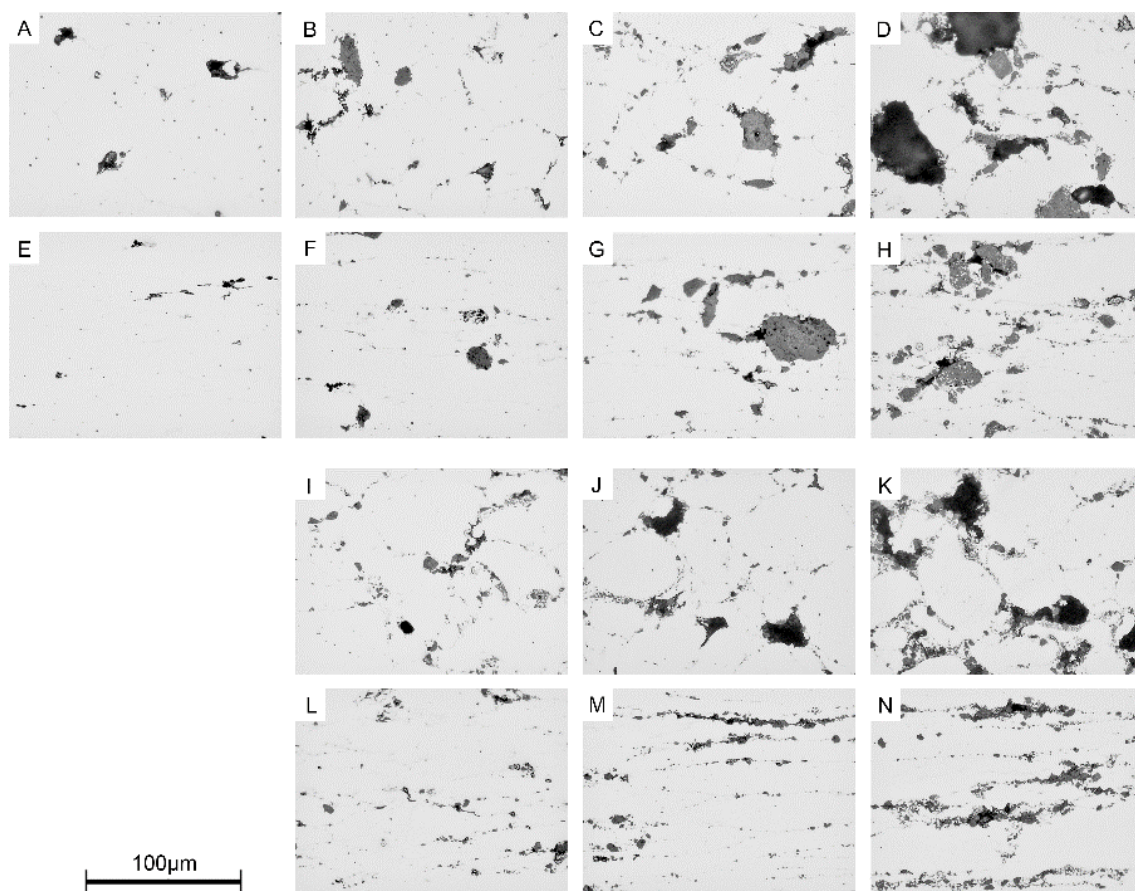


**Figure 3.** Sequence of unetched microstructures of as-sintered alloys (A) Base, (B) 2C, (C) 5C and (D) 10C contrasted by their hot worked counterpart in (E) base, (F) 2C, (G) 5C and (H) 10C. Additionally, a similar contrasting sequence of as sintered microstructures for (I) 2F, (J) 5F (K) 10F are shown with their forged counterparts in (L) 2F, (M) 5F and (N) 10F. All hot worked samples were processed at 400 °C and  $0.05 \text{ s}^{-1}$  to a strain of 0.70 mm/mm.

Hot worked microstructures are also shown in Figure 3; the base alloy (E) is contrasted by increasing concentration of coarse (F–H) or fine AlN additions (L–N). In all cases, the micrograph orientation is such that the loading direction was vertical. The Base alloy (Figure 3E) exhibited pore closure consistent with the direction of applied force. Similarly, prior particles were elongated in the direction transverse to this; prior particle boundaries were considerably less distinguishable

than the as-sintered base material. Unidentified secondary phases appear as dark gray features in these micrographs.

Hot worked alloy 2C (Figure 3F) exhibits pore closure like that of the Base alloy in that pores within the metallic matrix were heavily flattened while grains were flattened and elongated consistent with the deformation direction. In addition, pores were no longer observed in direct contact with AlN particles. The higher ceramic concentrations of 5C and 10C both exhibited microstructures (Figure 3G and H, respectively) where considerable residual porosity persisted adjacent to AlN particles after TMP, typically in dense AlN cluster formations where matrix penetration would be difficult in the solid state. However, pores were considerably smaller and less numerous than their as-sintered counterparts. In the forged 5C and especially the 10C microstructures, the shear forces on the matrix phase proved sufficient to separate AlN particulate that was not associated with dense clusters. These particles were essentially drawn out along what would have been the prior particle boundary. The benefit here was an increased homogeneity of the ceramic, which no longer strictly existed as features decorated along these prior particle boundaries. The result was less AlN-AlN particle contact. Evidence of AlN particle fracture was not observed in the microstructure of any deformed microstructures; the apparent breakup of fine AlN, particularly in AlN-F microstructures, can be wholly attributed to the redistribution of loosely bonded clusters of ceramic.

Microstructures of fine AlN 2F, 5F, and 10F after TMP are shown in Figure 3L, M, and N, respectively. Like their coarse counterparts, the microstructures exhibit pore flattening and ceramic redistribution from plastic deformation. Residual pores persisted alongside more complex clusters of ceramic particulate whereas cluster free regions exhibited minimal porosity. 5F and 10F showed obvious evidence of incomplete pore collapse. The deformation-induced flow of the metallic matrix within the ceramic network was also rather heterogeneous. In this sense, the AlN-F particulates were completely enveloped by the matrix in some areas but prevailed as porous clusters in others.

Despite the redistribution of ceramic particulate through TMP, ceramic-free regions persisted throughout the microstructure of all MMC compositions. These regions represent the interior of relatively large prior aluminum particles where conventional solid-state blending cannot invoke homogenization. Based on the density and microstructural data presented above, the alloys Base, 2C, 5C, 2F, and 5F were selected for constituent analysis. 10C and 10F were investigated less thoroughly due to their inferior performance.

Backscatter electron micrographs that illustrate grain evolution through TMP of Base, 2C, and 5C are shown in Figure 4. Immediately after sintering (Figure 4A–C), the grain size was largely consistent with the particle size of the starting aluminum powder while grain interiors showed no evidence of subgrains or misorientation gradients. It was postulated that the residual oxide phase between adjacent powder particles had likely provided a grain boundary pinning effect, thereby limiting the average grain size to one that was comparable to the  $D_{50}$  of the starting aluminum powder. Residual porosity and AlN particulate existed exclusively along these prior particle boundaries as is expected from a conventional PM process. The porosity was rounded and typically situated at triple junctions. The nature of the microstructures in Figure 4A–C remained remarkably similar despite the use of three different ceramic concentrations. The most notable difference was a lower indexing rate in the ceramic-bearing samples, as the AlN phase and porosity was not indexable. Following TMP, all materials, Figure 4D–F, showed extensive evidence of grain elongation and flattening consistent with the manner of applied strain. The nature of deformed grains remained reminiscent of the as-sintered microstructure, indicating that no recrystallization had occurred.

A summary of the grain boundary misorientation angles is provided in Table 2, expressed as the fraction ( $f$ ) of low angle grain boundaries (LAGBs). For convention, high angle grain boundaries (HAGBs) are defined as adjacent grain misorientation of  $15^\circ$  or greater. These are shown as black boundaries in Figure 4. Correspondingly, LAGBs have misorientation angles less than  $15^\circ$  but were not highlighted in Figure 4 for clarity. Local misorientation angles up to  $7^\circ$  were negated from this analysis due to issues arising from pseudo-symmetric misindexing. As-sintered samples exhibited

a microstructure largely devoid of LAGBs. Hence, HAGBs comprised the majority of the grain boundary area and it was likely that many of these were prior particle boundaries. On the other hand, hot deformed samples exhibited microstructures containing ~20–25% LAGBs. Furthermore, HAGBs appeared to remain along the prior particle boundaries of elongated grains while fine, equiaxed subgrains persisted within them. It is notable that subgrain boundaries are uniquely LAGBs.

**Table 2.** Fraction of low angle grain boundaries (misorientation  $\leq 15^\circ$ ) in the microstructures presented in Figure 4.

Condition	Material	fLAGB
As-Sintered	Base	0.02
	2C	0.06
	5C	0.04
Sintered + TMP	Base	0.18
	2C	0.18
	5C	0.24

**Table 3.** Summary of the material chemistries and TMP conditions found to induce circumferential cracking within the forged product.

TMP Condition (Temperature, Strain Rate)	Fractured Samples	Over-temperature ( $^\circ\text{C}$ )
500 $^\circ\text{C}$ , 5 $\text{s}^{-1}$	Base, 2C, 5C, 2F, 5F	+10.3, 8.7, 10.2, 8.7, 9.2
500 $^\circ\text{C}$ , 0.5 $\text{s}^{-1}$	5F	+1.8

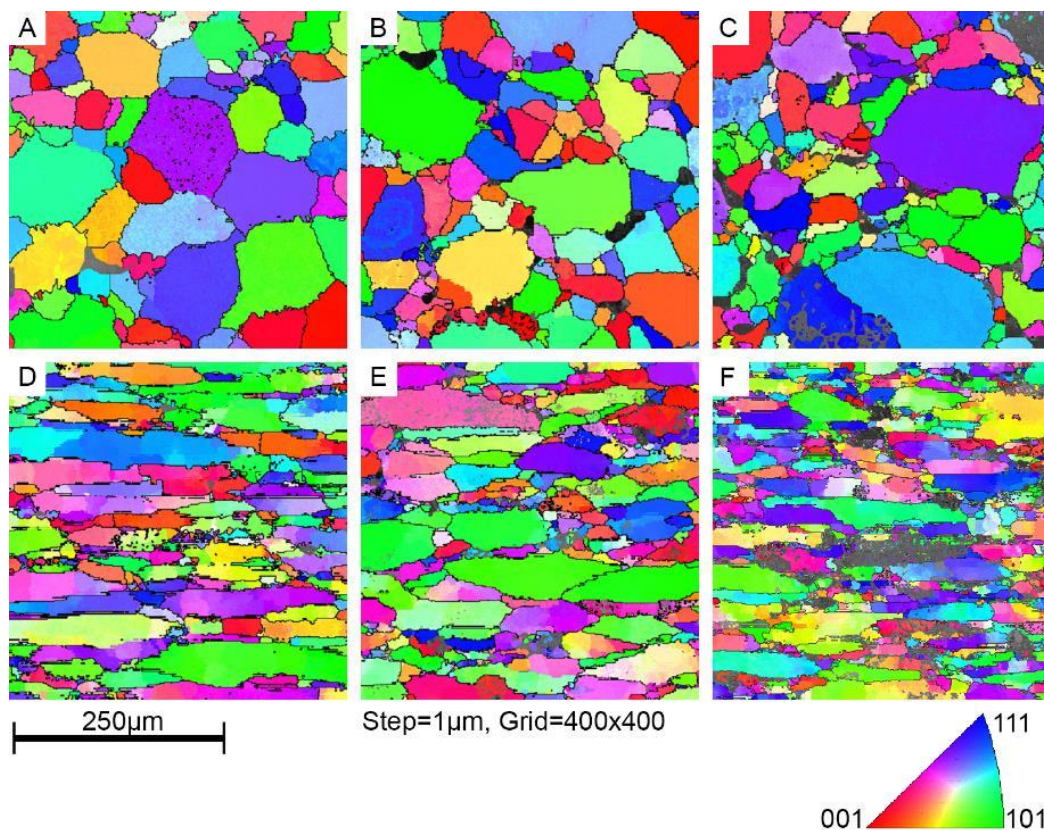


**Figure 4.** EBSD map of (A) Base, (B) 2C, and (C) 5C in the as sintered condition as well as variants deformed at 500  $^\circ\text{C}$  and 0.005  $\text{s}^{-1}$  for (D) Base, (E) 2C, and (F) 5C. TMP direction vertical with respect to page orientation.

Qualitative hot ductility assessments were made for all alloys. The clear majority of alloys under various TMP conditions proved to be sufficiently ductile to endure a true strain of 0.70 mm/mm. Samples that exhibited cracking are shown in Table 3. These cracks manifested at the outside circumference of the sample, and grew in the axial and radial directions. Cracking was only observed at the highest TMP temperature considered. At  $5 \text{ s}^{-1}$ , all tested samples experienced some degree of cracking. Note, 10C and 10F were not processed at such strain rates, and no such ductility assessment could be made. At  $0.5 \text{ s}^{-1}$ , the relatively porous 5F material similarly exhibited fine radial cracks. A micrograph of a crack initiation site at the surface of sample 2C can be seen in Figure 5, wherein the TMP direction was normal to the image. This intergranular crack path followed prior particle boundaries. This sample reached a peak temperature  $8.7 \text{ }^\circ\text{C}$  above the isothermal set point of  $500 \text{ }^\circ\text{C}$ . A comparable over-temperature was measured for all samples deformed using the same TMP conditions.

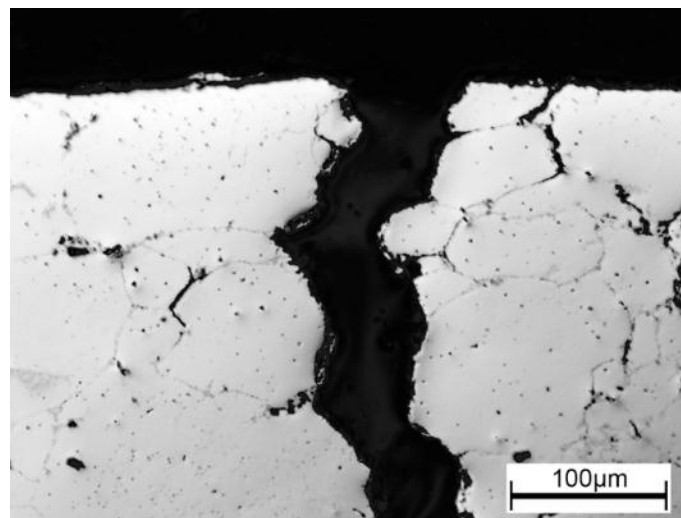


**Figure 5.** Typical appearance of cracks present at the circumference of select products after TMP. Sample 2C processed at  $500 \text{ }^\circ\text{C}$  and  $5 \text{ s}^{-1}$ . TMP direction was normal to the plane of the image.

### 3.3. Flow Curves

Representative flow stress curves for MMC 2C are shown in Figure 6. Flow curves for all other material compositions are not included as the trends were largely comparable with these exemplary plots. Generally, the material exhibited a peak flow stress at low strain followed by a monotonic decay commensurate with ‘flow softening’. At low temperatures and high strain rates, this phenomenon was more apparent. When TMP was executed at  $350 \text{ }^\circ\text{C}$  and  $0.005 \text{ s}^{-1}$ , the flow stress exhibited a monotonic decrease from a peak of  $94.4 \text{ MPa}$  to  $68.5 \text{ MPa}$  at a strain of  $0.65 \text{ mm/mm}$ . Conversely, samples deformed at  $5 \text{ s}^{-1}$  and temperatures  $\geq 450 \text{ }^\circ\text{C}$  exhibited a short period of strain where peak flow stress and softening were observed. Afterwards, the flow stress values remained effectively static. An exemplary case is the sample deformed at the same strain rate as the aforementioned sample,  $0.005 \text{ s}^{-1}$ , but now at  $500 \text{ }^\circ\text{C}$ . A peak in flow stress ( $23.6 \text{ MPa}$ ) followed by a rapid flow softening of  $24.7\%$  (to  $17.7 \text{ MPa}$ ) was observed at a strain of only  $0.054 \text{ mm/mm}$ , followed by an additional, albeit marginal, softening of  $6.4\%$  (to  $16.6 \text{ MPa}$ ) from strain values of  $0.054 \text{ mm/mm}$  to  $0.65 \text{ mm/mm}$ . Overall, moderate levels of softening were exhibited at all temperatures for all samples, but the rate of softening varied closely with TMP temperature and strain rate.

The peak flow stress behavior of the alloy as a function of ceramic content, TMP temperature, and strain rate are shown in Table 4. For a given temperature and strain rate, the peak flow stress values remained largely equivalent for all alloy compositions considered. Differences between compositions Base, 2C, 5C, and 2F were especially small. For example, at  $400 \text{ }^\circ\text{C}$  and  $0.500 \text{ s}^{-1}$ , the peak stress values

only ranged from 100.7 MPa to 100.9 MPa while the average range for any set of TMP conditions was just 4.5 MPa. Interestingly, the 5F composition exhibited peak flow stresses distinct from the other compositions. Again at 400 °C and 0.500 s<sup>-1</sup>, this specific composition exhibited a peak flow stress of 96.3 MPa. The change in peak flow stress value for a given composition was influenced by both temperature and strain rate. A decrease in strain rate or an increase in temperature both corresponded to a decrease in flow stress. For the range of TMP conditions considered, the flow stress appears to be influenced more strongly by temperature.

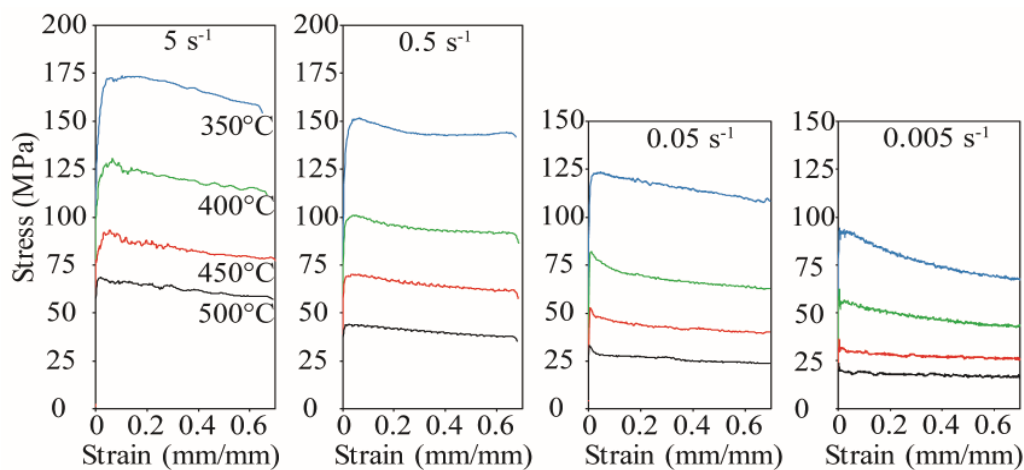


**Figure 6.** Flow stress (true stress—true strain) curves for alloy 2C developed during TMP at temperatures of 350 °C to 500 °C and strain rates of 5 s<sup>-1</sup>, 0.5 s<sup>-1</sup>, 0.05 s<sup>-1</sup> and 0.005 s<sup>-1</sup>.

**Table 4.** Effects of TMP conditions and material composition on the peak flow stress.

Composition	True Strain Rate, Nominal (s <sup>-1</sup> )	TMP Temperature, Nominal (°C)			
		350	400	450	500
Base	5.000	175.8	131.4	100.2	69.6
2C		173.5	130.7	93.2	68.7
5C		176.6	131.0	101.1	71.0
2F		169.3	129.8	100.3	70.5
5F		158.0	113.2	83.9	58.5
Base	0.500	147.2	100.8	72.8	45.1
2C		151.8	100.9	70.3	44.1
5C		148.3	100.7	66.6	45.1
2F		153.6	100.7	69.2	45.5
5F		130.5	96.3	60.8	40.5
Base	0.050	125.3	78.7	48.7	30.6
2C		123.4	81.9	52.8	33.3
5C		121.7	81.3	54.3	31.5
2F		124.9	76.3	50.5	32.1
5F		111.6	70.2	45.1	27.0
Base	0.005	98.4	63.5	42.3	21.9
2C		94.4	62.3	36.2	23.6
5C		99.4	65.2	38.7	22.6
2F		102.4	63.7	32.9	21.7
5F		89.1	57.9	31.9	21.0

In the next stage of work, the effects of extended furnace soaking prior to TMP were briefly assessed. Work was constrained to MMC 5F deformed at 350 °C or 450 °C and a strain rate of 0.05 s<sup>-1</sup>

with an extended isothermal hold of 150 s. Flow curves for these samples are shown with their 15 s isothermal hold counterparts in Figure 7. The difference in flow stress at any given strain (above 0.01 mm/mm) at 350 °C was approximately 15 MPa to 20 MPa. Accordingly, an extended isothermal hold substantially decreased the load required to deform the sample. To contrast this, the difference at 450 °C was much less notable. Up to a true compressive strain of 0.5 mm/mm, the difference in flow stress for any given strain value was only 1 MPa to 3 MPa.

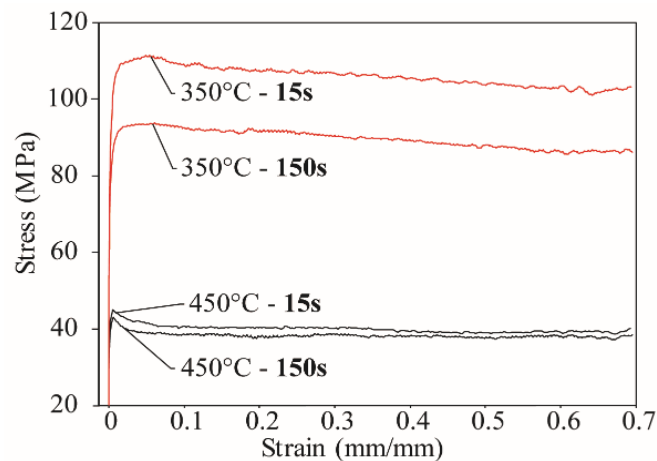


**Figure 7.** Data illustrating the effects of isothermal hold time on the flow curves for MMC 5F when deformed at 350 °C and 450 °C. A strain rate of  $0.05 \text{ s}^{-1}$  was employed in all instances.

## 4. Discussion

### 4.1. Porosity

In general, additions of either ceramic type began to inhibit sintering once a critical volume fraction threshold was surpassed. At a concentration of 2% vol, the sintered density was effectively identical to that of the ceramic-free Base alloy. Since ceramic particles lie along prior particle boundaries, this particular concentration appeared to be sufficiently low to minimize AlN-AlN interaction allowing for adequate separation amongst discrete ceramic particles. This lack of AlN interaction was exhibited in Figure 3B–I wherein ceramic clustering was minimized and near full density was achieved directly after sintering. Increased ceramic additions saturated prior particle boundary regions with AlN particles. Once saturated, AlN-AlN interaction became progressively more pronounced with rising ceramic contents. This increase in AlN-AlN interaction was exemplified in the string of micrographs of AlN-C in Figure 3B–D. Pores were a direct result of the inability of the matrix to penetrate these complex ceramic clusters. This phenomena has been explained in a previous study with comparable powders and blending conditions [18] as large concentrations of a fine particle size AlN were susceptible to clustering, introducing localized pore networks. Alloys containing AlN-F invariably contained a larger number of discrete AlN particles for a given volume fraction. Saturation of the grain boundaries with these finer particles must thereby occur at a lower concentration than that observed with AlN-C. This was first noted as a difference in density at 5% ceramic content. Here, 5C sintered to 98.4% and exhibited some ceramic-free prior particle boundaries (Figure 3C). 5F, on the other hand, was only 95.2% dense and exhibited prior particle boundaries (Figure 3J) that appeared more crowded with clustered ceramic.

Forged densities significantly exceed their precursory as-sintered values by way of pore collapse. Shear strain elongated and flattened the pores in the transverse direction. The compositions of Base, 2C, 5C, and 2F all densified by approximately the same amount, from 0.6% to 1.0% above their as-sintered values. Incidentally, these are the samples that did not exhibit excessive AlN-AlN interaction along prior particle boundaries. In the absence of a significant amount of porosity from

this effect, TMP-induced densification was largely attributable to the collapse of residual porosity inherent to the matrix. Considering compositions where ceramic clustering was evident (10C, 5F, and 10F), densification as a result of thermal-mechanical processing was more substantial in light of their lower sintered densities, and in turn, the availability of collapsible pores. However, residual, partially-collapsed pores prevailed in the hot forged samples, routinely appearing within dense, complex AlN clusters, as shown in Figure 3H, M, N). Evidently, the amount of strain imparted on samples was insufficient to redistribute AlN particles such that the matrix phase could penetrate the pores adequately.

#### 4.2. Hot Ductility

In an MMC system with a heat-treatable matrix, ductility may be adversely impacted through decohesion of the particle/matrix interface [17] and/or preferential precipitate formation/growth along grain boundaries [19]. However, these explanations were deemed insufficient in this study as cracking only occurred at relatively high strain rates and hot working temperatures. It was thereby postulated that deformation-induced heating was the principal factor of influence. In this sense, under rapid strain rates, the self-heating of the material instilled through deformation could not be accommodated quickly enough within the closed-loop temperature control system of the Gleeble. This led to moderate over-heating (Table 3) such that the peak temperatures were now in close proximity to the incipient melting point of the Base alloy (520 °C [20]). The authors thereby inferred that this had caused hot shortness that was manifested as cracking of the forged product. This problem did not occur at lower strain rates of  $0.05\text{ s}^{-1}$  and  $0.005\text{ s}^{-1}$ . Here, superior temperature control was maintained as thermal overshoot was  $<1\text{ °C}$  during deformation. This avoided onset of hot shortness and yielded crack-free products.

#### 4.3. Flow Behavior

Evidence in this paper insinuated that the flow behavior of the materials was consistent with DRV. The forged microstructures exhibited grains elongated transverse to the TMP direction. No equiaxed grains with HAGBs were observed. LAGB boundaries were rampant; many finer, equiaxed, subgrains were observed within deformed 'prior particles'. Dynamic recrystallization is therefore ruled out, and DRV is concluded to be operative. However, the flow-softening behavior exhibited under most deformation conditions in Figure 6 deviates from normal DRV curves. This discrepancy is attributable to dynamic precipitation (DPN). Simultaneous DRV and DPN mechanisms have been previously observed in other heat treatable APM materials [9] as well as the 2xxx series wrought aluminum alloy system [19]. In DPN, thermally motivated precipitates can form and strengthen the material in-situ leading to a rise in flow stress under certain conditions. However, if thermal exposure is adequately prolonged, overaging and a concomitant decrease in the strengthening effect transpires (manifested as a decreased flow stress). This thermal exposure can be in-situ or prior to deformation. Deformation at relatively low temperatures prompts the nucleation and growth of more and finer strengthening precipitates. However, as solid solubility rises with increasing deformation temperature, the driving force for precipitate formation decreases. This can invoke the dissolution of early-stage precipitates as well as rapid coarsening of those that are larger and more mature. Those that remain are now less effective at strengthening such that reduced flow stresses are now needed to instill plastic deformation.

DPN effects are directly influenced by the microstructure of the material prior to deformation. This fact was particularly important in the current study as all thermal-mechanical testing was applied to specimens in the 'as-sintered' condition. In this state, Al-Cu-Mg APM alloys are known to contain a rather unique compilation of strengthening precipitates that includes phases from the complete precipitation sequence. This is driven by the temperature employed in sintering and the ensuing rate at which the specimens were cooled from this temperature. In this sense, all specimens were sintered at 600 °C. This was above the alloy solidus and thereby ensured that a small amount of liquid phase enriched in alloying additions existed in the material at this temperature. Sintered parts

were then cooled in a semi-accelerated manner as they were conveyed into a water jacketed segment of the furnace under high rates of flowing nitrogen. The associated cooling rate is reasonably fast (i.e., 1 °C/s) at temperatures >200 °C, but is reduced to a tenth of this value for the remainder of the cooling profile [21]. The resultant microstructure thereby includes solidified remnants of the liquid phase and  $\alpha$ -Al grains that contain phases from the entire precipitation sequence, including incoherent equilibrium precipitates and even a solid solution component that dissociates during natural aging of the finished product [22]. Now considering the flow-softening behavior exhibited in Figure 6, it is apparent this was driven by the combination of deformation temperature and strain rate. First, consider the contrasting behavior of curves corresponding to 350 °C and 500 °C for the strain rate of 0.005 s<sup>-1</sup> in Figure 6. At 350 °C, the supersaturation is relatively high, so the driving force for new strengthening precipitates was accordingly high. Flow-softening here was largely attributable to the loss in strength due to these in-situ forming precipitates. At 500 °C, no appreciable supersaturation exists. No precipitation occurs in situ and minimal flow softening occurs. The explanation for the flow softening exhibited for samples deformed at 500 °C and deformed at higher strain rates is attributable to pre-existing precipitates. These precipitates are inherent to the sintered microstructure and provide marginal strengthening effects. Again, overaging of these pre-existing precipitates during deformation reduces their strength contribution.

Further proof of the influence of DPN was devised through the elongated isothermal hold tests of Figure 7. The corresponding DSC trace of 2C in the T1 condition has been previously studied by the authors [20]. Upon heating to 350 °C and prior to deformation, the material has gone through several microstructural events, most notably static precipitation of the Type-I and/or Type -II S phase (DSC event peak at approximately 320 °C) [23]. Extended thermal exposure at 350 °C thereby fosters the growth and coarsening of all pre-existing precipitates present. These coarser precipitates provide less resistance towards dislocation motion. Both 15 s and 150 s holds at this temperature exhibit ongoing work softening at approximately the same rate, indicating that in both instances, precipitate growth (DPN) remains operative. At ~375 °C, dissolution of the S phase precipitates commences. This reaction then continues until a temperature of approximately 505 °C. Throughout this event, strengthening precipitates are dissolved into the matrix to a progressively greater extent. In the relative absence of precipitates, the flow stress behavior of both samples processed at 450 °C naturally converged, although the sample with extended hold time did show a marginally lower flow stress. As strain increased, the flow stresses remained different by approximately 1 MPa to 2 MPa. It is notable that the effects of solute drag as a result of this dissolution event are anticipated to be minimal as demonstrated in a study on a chemically comparable 2xxx series alloy [19].

Aside from DPN, ceramic content also influenced the peak flow stress. This was particularly acute at low strain values, as a definitive trend with the MMC composition emerged. For instance, as shown below in Figure 8, peak flow stresses were consistently higher in MMCs that were relatively lean in ceramic content but declined proportionately as the ceramic content increased. Such transitions were somewhat counter-intuitive to what may be expected through the addition of a rigid phase, as reported for other aluminum MMC systems [16]. However, it was consistent irrespective of the use of AlN-C or AlN-F. For instance, the base alloy yielded at 126 MPa, while 2C and 2F were marginally softer, with peak flow stresses 3 MPa and 1 MPa lower, respectively. 5C again exhibited only a marginal reduction in flow stress, 4 MPa weaker than Base. Considerable differences in flow stresses were then observed for 10C and 10F, which are 18 MPa and 21 MPa softer. 5F exhibited an intermediate softening of 14 MPa. The root cause for this behavior lied in differences amongst the sintered densities of the preforms. The sintered density and ceramic content are highly correlated (i.e., correlation factor  $-0.942$ ,  $p$ -value 0.000). Increased ceramic additions inherently limited the sintered density and these changes were manifested in the flow curves as slightly weaker materials. For the Gleeble samples deformed at 0.05 s<sup>-1</sup>, these trends can be observed in Figure 9. In all cases, the positive, nonzero linear relationship was highly significant, and sintered density explained most of the variance in peak flow stress (R-sq and  $p$ -values for the linear trends at 500 °C, 450 °C, 400 °C and 350 °C: 82.2 and 0.005, 78.6 and 0.008,

80.1 and 0.006, 93.7 and 0.000). These findings are consistent with the precedent that sintered preforms with a high relative density will yield at relatively high stress while those that are more porous yield at lower stresses [12]. When accounting for the sintered density of the materials, the influence of the ceramic type and concentration was not statistically significant. Following suit, the convergent behavior of flow stress curves following the peak may be attributed to dynamic densification effects.

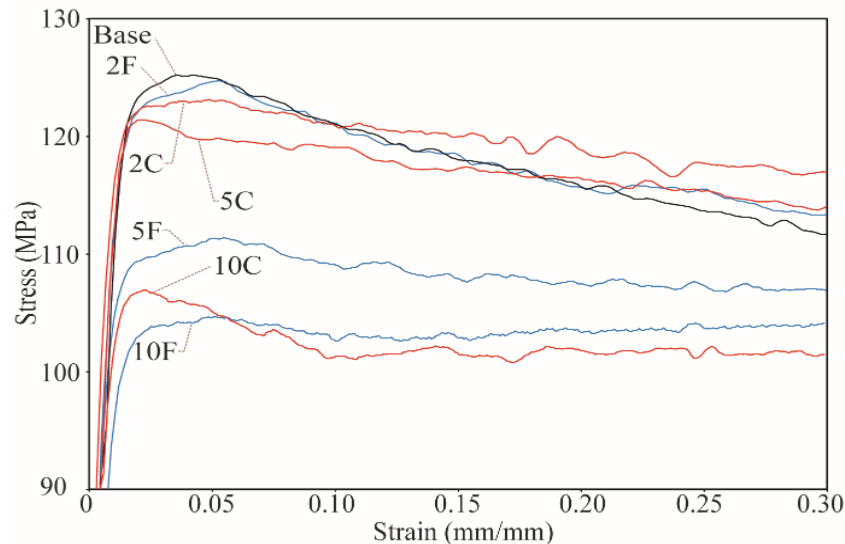


**Figure 8.** Flow curves for each material composition deformed at 350 °C and 0.05 s<sup>-1</sup> exhibiting the variation in peak flow stress.

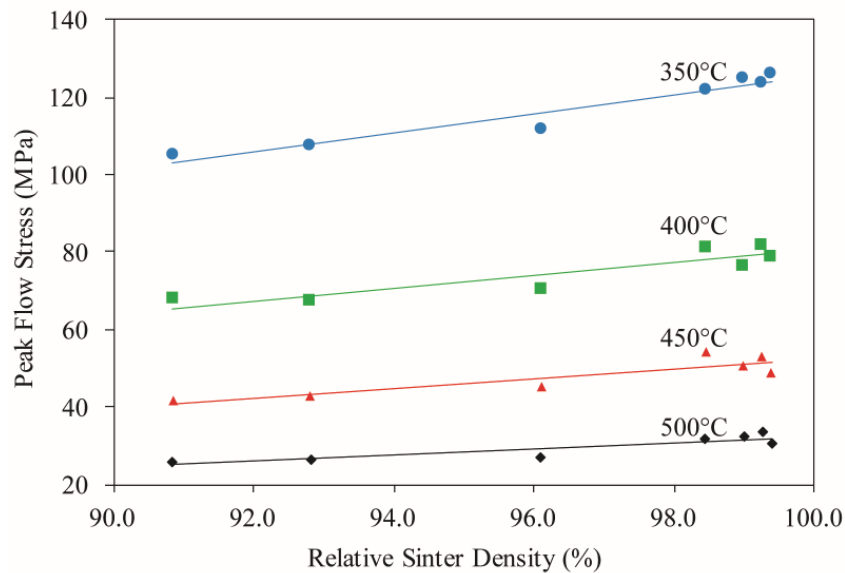


**Figure 9.** Effect of preform sintered density on the peak flow stress; samples deformed at a strain rate of 0.05 s<sup>-1</sup> and temperatures 350 °C to 500 °C.

#### 4.4. Constituent Analysis

The sinh Zener-Hollomon constituent analysis approach was successfully applied to the majority of materials used in this study, except for 10C and 10F compositions, which were excluded from this phase due to their limited number of test conditions. Resultant constituent values are summarized in Table 5. It should be noted that the calculated value of  $\alpha$  was found to vary slightly depending on the material composition. A common value of  $\alpha$  (0.016 MPa<sup>-1</sup>) was selected from the list of calculated

values which best-suited the family of materials. In literature, a larger  $\alpha$  ( $0.052 \text{ MPa}^{-1}$ ) is commonly chosen [15]; however, in this case, it proved to poorly represent data at extreme Z values.

**Table 5.** Constituent values for the APM materials modeled in accordance with Equation (1).

	$\alpha$ ( $\text{MPa}^{-1}$ )	n	S	$Q_{\text{HW}}$ (kJ/mol)	$\ln(A)$ ( $\text{s}^{-1}$ )
BASE	0.016	5.4	2619	272	42.5
2C	0.016	5.6	2622	279	43.7
5C	0.016	5.5	2649	277	43.5
2F	0.016	5.4	2626	271	42.6
5F	0.016	6.0	2543	292	46.8

The activation energy of hot working,  $Q_{\text{HW}}$ , provides valuable insight into the forging behavior of these materials. In terms of absolute performance, the base material shows the same elevated level of temperature sensitivity characteristic of comparable age-hardenable aluminum alloys in the solutionized state [19]. This was no doubt attributed to the T1 state of the starting material, as the presence of alloying elements in solid solution and/or highly underaged precipitates allows for DPN. Here, low temperature strength of the materials is elevated through in-situ precipitation, while elevated temperature deformation more easily circumvents these strengthening effects. As alluded to earlier, a precursory isothermal hold reduced DPN effects, minimizing the temperature sensitivity of the material and reducing  $Q_{\text{HW}}$  [14]. Comparatively, differences in  $Q_{\text{HW}}$  may be attributed to the strengthening effects provided through varying ceramic content. Ceramic-bearing alloys typically show a temperature sensitivity from the inefficient recovery mechanisms of the matrix phase being able to cope with the increased dislocation densities at low temperatures. Whereas at more elevated temperatures, recovery becomes sufficiently efficient and flow behavior rivals that of the matrix phase. Here, differences in activation energy between materials were subtle. Base, 2C, 5C, and 2F all exhibited comparable  $Q_{\text{HW}}$  values. Notably, 5F possessed the highest  $Q_{\text{HW}}$  and n. Peak flow stresses were routinely less than those of Base, 2C, 5C, or 2F because of the porosity negatively impacting mechanical strength. The magnitude of change in flow stress arising from this was most notable at lower temperatures and higher strain rates.

Figure 10 plots the calculated peak flow stress values versus strain rate for the range of temperatures observed in this study. In addition, the experimental values for the corresponding TMP parameters are superimposed to show their adherence to the Zener-Hollomon analyses. In general terms, the alloys Base, 2C, 5C, and 2F performed similar enough to justify characterizing them as a single material type. Consequently, a single curve represents these four sets of data points. 5F was represented by its own set of unique curves per its regression. This plot serves as a useful tool in predicting the forging behavior of these materials for any combination of temperature and strain rate within the boundaries considered. The deformation response of these ceramic materials can be largely attributed to the density to which they are processed prior to sintering. Given comparable degrees of densification, the effects of the type and amount of ceramic content were negligible.

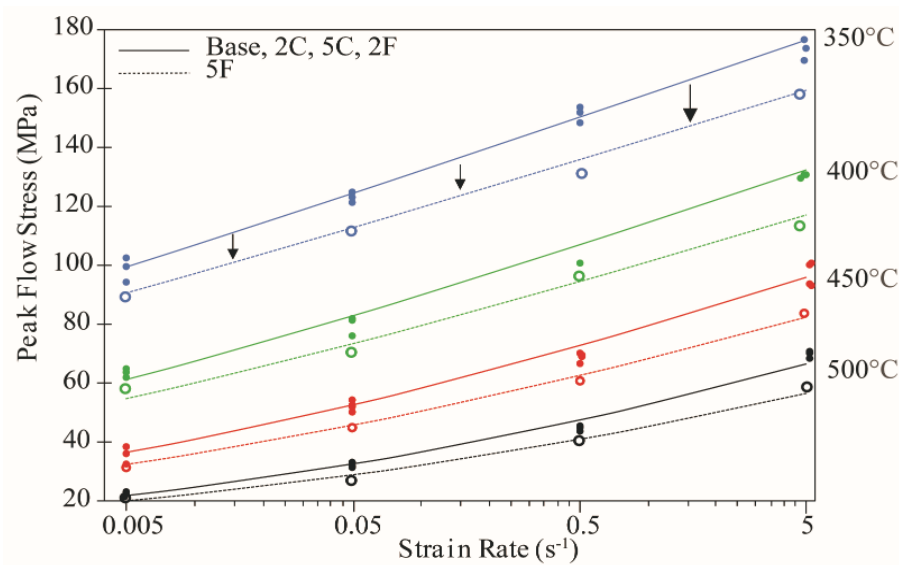


**Figure 10.** Peak flow stress data for MMC materials plotted versus strain rate. Experimental data points superimposed on Zener-Hollomon calculated curves (solid and dashed lines).

## 5. Conclusions

TMP studies were successfully performed on a variety of sintered APM materials containing varied amounts of AlN additions. Press-and-sinter samples were hot-worked in the as-sintered (T1) condition at temperatures ranging from 350 °C to 500 °C, and strain rates of 0.005 s<sup>-1</sup> to 5 s<sup>-1</sup>. All samples were deformed to a strain of 0.70 mm/mm. The hot formability of these materials could be quantified through density measurements, metallography and Zener-Hollomon analyses. In general, the stress strain flow curves showed work-hardening followed by either a steady-state flow stress or work softening. More specifically, it can be concluded that:

- The density of all materials invariably increased through TMP. However, temperature and strain rate did not influence final density values significantly. Samples that were sintered to near-theoretical density (>99.0%), including Base, 2C, and 2F alloys, were forged to essentially full density (>99.9%). Samples with an inferior sintered density did not reach their respective full density values.
- Samples deformed at 500 °C were susceptible to cracking. Deformation facilitated *in-situ* heating beyond the targeted temperature under select circumstances that led to crack growth along prior particle boundaries. The lower sintered density of MMC 5F also appeared to be influential.
- Static and dynamic precipitation were exhibited throughout the deformation conditions considered. The effects of DPN were evident below the solvus, especially at the lowest deformation temperature. Temperatures of 450 °C and higher exhibited evidence of precipitate dissolution, encouraging lower flow stresses.
- The implementation of isothermal holds confirmed the occurrence of precipitation events. Increased isothermal hold time allowed for precipitate coarsening and an associate reduction in flow stress. At 450 °C, near-equilibrium flow stresses were approached within 15 s. At 350 °C, slower kinetics were apparent and softening occurred with 150 s isothermal hold prior to deformation.
- Additions of AlN that negatively impacted sintered density also decreased flow stress. This effect was most acute when AlN-F additions were employed.
- Zener-Hollomon analyses using a sinh approach enabled the peak flow stress characteristics of BASE, 2C, 5C, 2F, and 5F systems to be mapped. The results were effectively identical for all systems except the 5F formulation wherein a clear difference emerged.

**Author Contributions:** Conceptualization, D.P.B. and M.A.W.; Data curation, G.A.W.S.; Formal analysis, G.A.W.S. and D.P.B.; Funding acquisition, D.P.B.; Investigation, G.A.W.S.; Methodology, G.A.W.S., D.P.B. and M.A.W.; Project administration, A.T.; Resources, M.A.W., R.L.H. and I.W.D.; Supervision, D.P.B.; Writing—original draft, G.A.W.S. and D.P.B.; Writing—review & editing, G.A.W.S., D.P.B., M.A.W., A.T., R.L.H. and I.W.D.

**Funding:** This research was funded by the Natural Sciences and Engineering Research Council of Canada (NSERC) via the Collaborative Research & Development grant CRDPJ, number [486528-15].

**Acknowledgments:** The authors would like to acknowledge Bernhard Mais (Ecka Granules) and Jessu Joys (U.S. Metal Powders) are acknowledged for the provision of the powdered metals employed.

**Conflicts of Interest:** The authors declare no conflict of interest.

## References

1. Kim, Y.W.; Griffith, W.M.; Froes, F.H. Surface Oxides in P/M Aluminum-Alloys. *J. Met.* **1985**, *37*, 27–33. [[CrossRef](#)]
2. Schaffer, G.B.; Sercombe, T.B.; Lumley, R.N. Liquid phase sintering of aluminium alloys. *Mater. Chem. Phys.* **2001**, *67*, 85–91. [[CrossRef](#)]
3. Xie, G.; Ohashi, O.; Song, M.; Mitsuishi, K.; Yasuda, H.; Furuya, K.; Noda, T. Electron microscopic observation of interfaces of aluminium powder compacts prepared by spark plasma sintering. *J. Electron. Microsc.* **2002**, *51*, S149–S153. [[CrossRef](#)]
4. Yi, J.Z.; Gao, Y.X.; Lee, P.D.; Flower, H.M.; Lindley, T.C. Scatter in fatigue life due to effects of porosity in cast A356-T6 aluminum-silicon alloys. *Metall. Mater. Trans. A* **2003**, *34*, 1879–1890. [[CrossRef](#)]
5. James, W.B. Powder Forging. *Rev. Part. Mater.* **1994**, *2*, 173–214.
6. Dashwood, R.; Schaffer, G. Powder forging of a sintered Al–3.8Cu–1Mg–0.8Si–0.1Sn alloy. *Mater. Sci. Eng. A* **2002**, *323*, 206–212. [[CrossRef](#)]
7. Park, J.-O.; Kim, K.-J.; Kang, D.-Y.; Lee, Y.; Kim, Y.-H. An experimental study on the optimization of powder forging process parameters for an aluminum-alloy piston. *J. Mater. Process. Technol.* **2001**, *113*, 486–492. [[CrossRef](#)]
8. Asgharzadeh, H.; Simchi, A.; Kim, H.S. Dynamic restoration and microstructural evolution during hot deformation of a P/M Al6063 alloy. *Mater. Sci. Eng. A* **2012**, *542*, 56–63. [[CrossRef](#)]
9. Mosher, W.G.E.; Kipourous, G.J.; Caley, W.F.; Donaldson, I.W.; Bishop, D.P. On hot deformation of aluminium-silicon powder metallurgy alloys. *Powder Metall.* **2011**, *54*, 366–375. [[CrossRef](#)]
10. Bose, A.; Eisen, W.B. *Hot Consolidation of Powders & Particulates*; Metal Powder Industries Federation: Princeton, NJ, USA, 2003; ISBN 1878954490.
11. Committee, A.I.H. *ASM Handbook, Volume 07—Powder Metal Technologies and Applications*; ASM International: Materials Park, OH, USA, 1998; ISBN 978-0-87170-387-3.
12. Abdel-Rahman, M.; El-Sheikh, M.N. Workability in forging of powder metallurgy compacts. *J. Mater. Process. Technol.* **1995**, *54*, 97–102. [[CrossRef](#)]
13. Altan, T.; Ngaile, G.; Shen, G. *Cold and Hot Forging: Fundamentals and Applications, Volume 1*; ASM International: Materials Park, OH, USA, 2005; ISBN 0871708051.
14. Mcqueen, H.J.; Spigerelli, S.; Kassner, M.E.; Evangelista, E. Chapter 4. Hot Working of Aluminum. In *Hot Deformation and Processing of Aluminum Alloys*; CRC Press: Boca Raton, FL, USA, 2011; pp. 36–42.
15. Mcqueen, H.J.; Ryan, N. Constitutive analysis in hot working. *Mater. Sci. Eng. A* **2002**, *322*, 43–63. [[CrossRef](#)]
16. McQueen, H.J.; Zhao, J.; Sauerborn, M. Constitutive Analysis, Extrusion Modeling of 2618 Particulate Composites. In *Processing and Fabrication of Advanced Materials X*; Srivatsan, M., Varin, R., Eds.; ASM Intl: Cleveland, OH, USA, 2002; pp. 467–472.
17. Mcqueen, H.J.; Spigerelli, S.; Kassner, M.E.; Evangelista, E. Chapter 7. Aluminum Matrix Composites. In *Hot Deformation and Processing of Aluminum Alloys*; CRC Press: Boca Raton, FL, USA, 2011.
18. Sweet, G.A.; Brochu, M.; Hexemer, R.L.; Donaldson, I.W.; Bishop, D.P. Consolidation Of Aluminum-Based Metal Matrix Composites Via Spark Plasma Sintering. *Mater. Sci. Eng. A* **2015**. [[CrossRef](#)]
19. Mcqueen, H.J.; Spigerelli, S.; Kassner, M.E.; Evangelista, E. Chapter 6. Precipitation Hardening Alloys. In *Hot Deformation and Processing of Aluminum Alloys*; CRC Press: Boca Raton, FL, USA, 2011.

20. Sweet, G.A.; Bishop, D.P.; Williams, B.W.; Taylor, A.; Hexemer, R.L.; Donaldson, I.W. Development of a process to investigate the mechanical properties of a powder forged aluminum alloy. In *Powdermet 2017*; MPIF: Las Vegas, NV, USA, 2017.
21. Hennessey, C.W.; Caley, W.F.; Kipouros, G.J.; Bishop, D.P. *Development of a PM Aluminum Alloy: Effect of Post-Sinter Cooling Conditions*; American Powder Metallurgy Institute: Princeton, NJ, USA, 2006; Volume 42.
22. Bishop, D.P.; McNally, R.L.; Geiman, T.E. Metallurgical considerations in the manufacture and development of aluminum P/M camshaft bearing caps. In *Proceedings of the 2nd Powder Metallurgy Aluminum & Light Alloys for Automotive Applications Conference*, Troy, MI, USA, November 2–3 2000; Metal Powder Industries Federation: Princeton, NJ, USA, 2000; pp. 177–185.
23. Parel, T.S.; Wang, S.C.; Starink, M.J. Hardening of an Al-Cu-Mg alloy containing Types I and II S phase precipitates. *Mater. Des.* **2010**, *31*, S2–S5. [[CrossRef](#)]



© 2018 by the authors. Licensee MDPI, Basel, Switzerland. This article is an open access article distributed under the terms and conditions of the Creative Commons Attribution (CC BY) license (<http://creativecommons.org/licenses/by/4.0/>).